

RESEARCH ARTICLE

10.1002/2014JD022834

Key Points:

- Black carbon-containing particles are characterized via mass spectrometry
- Comparison with a colocated standard mass spectrometer is presented
- Approximately 35% of the measured submicron aerosol mass contains black carbon

Supporting Information:

- Texts 1–7 and Figures S1–S10

Correspondence to:

P. Massoli,
pmassoli@aerodyne.com

Citation:

Massoli, P., et al. (2015), Characterization of black carbon-containing particles from soot particle aerosol mass spectrometer measurements on the R/V *Atlantis* during CalNex 2010, *J. Geophys. Res. Atmos.*, 120, 2575–2593, doi:10.1002/2014JD022834.

Received 10 NOV 2014

Accepted 24 FEB 2015

Accepted article online 28 FEB 2015

Published online 28 MAR 2015

Characterization of black carbon-containing particles from soot particle aerosol mass spectrometer measurements on the R/V *Atlantis* during CalNex 2010

Paola Massoli¹, Timothy B. Onasch¹, Christopher D. Cappa², Ibraheem Nuamaan^{3,4}, Jani Hakala⁵, Katherine Hayden³, Shao-Meng Li³, Donna T. Sueper^{1,6}, Timothy S. Bates^{7,8}, Patricia K. Quinn⁸, John T. Jayne¹, and Douglas R. Worsnop¹

¹Aerodyne Research Inc., Billerica, Massachusetts, USA, ²Department of Civil and Environmental Engineering, University of California, Davis, California, USA, ³Air Quality Research Division, Environment Canada, Toronto, Ontario, Canada, ⁴Centre for Atmospheric Chemistry, York University, Toronto, Ontario, Canada, ⁵Department of Physics, University of Helsinki, Helsinki, Finland, ⁶Department of Chemistry and Biochemistry, University of Colorado Boulder, Boulder, Colorado, USA, ⁷Joint Institute for the Study of the Atmosphere and Ocean, University of Washington, Seattle, Washington, USA, ⁸NOAA Pacific Marine Environmental Laboratory, Seattle, Washington, USA

Abstract We present mass spectrometry measurements of black carbon-containing particles made on board the R/V *Atlantis* during the CalNex (California Research at the Nexus of Air Quality and Climate Change) 2010 study using an Aerodyne Research Inc. soot particle aerosol mass spectrometer (SP-AMS). The R/V *Atlantis* was deployed to characterize air masses moving offshore the California coast and to assess emissions from sources in urban ports. This work presents a first detailed analysis of the size-resolved chemical composition of refractory black carbon (rBC) and of the associated coating species (NR-PM_{BC}). A colocated standard high-resolution aerosol mass spectrometer (HR-AMS) measured the total nonrefractory submicron aerosol (NR-PM₁). Our results indicate that, on average, 35% of the measured NR-PM₁ mass (87% of the primary and 28% of the secondary NR-PM₁, as obtained from the mass-weighted average of the NR-PM_{BC} species) was associated with rBC. The peak in the average size distribution of the rBC-containing particles measured by the SP-AMS in vacuum aerodynamic diameter (d_{va}) varied from ~100 nm to ~450 nm d_{va} , with most of the rBC mass below 200 d_{va} . The NR-PM_{BC} below 200 nm d_{va} was primarily organic, whereas inorganics were generally found on larger rBC-containing particles. Positive matrix factorization analyses of both SP-AMS and HR-AMS data identified organic aerosol factors that were correlated in time but had different fragmentation patterns due to the different instruments vaporization techniques. Finally, we provide an overview of the volatility properties of NR-PM_{BC} and report the presence of refractory oxygen species in some of the air masses encountered.

1. Introduction

Atmospheric aerosol particles have important impacts on visibility, human health, and climate [Intergovernmental Panel on Climate Change, 2013]. Refractory black carbon (rBC)-containing particles, often referred to as soot, are emitted from incomplete combustion processes, are strong light absorbers in the visible and near visible wavelengths, and have been recognized as potentially important players in climate forcing through direct warming and alteration of cloud properties [Jacobson, 2001, 2006; Ramanathan et al., 2007; Ramanathan and Carmichael, 2008; Bauer et al., 2010; Shindell et al., 2012; Bond, 2007; Bond et al., 2013]. Understanding the transformations that rBC-containing particles undergo in the atmosphere after emission is key to accurately describing and modeling the radiative effects of rBC. It is well known that aging of rBC can occur through coagulation and condensation of organic and inorganic components (or coating material), which can be mildly light absorbing or nonabsorbing. As the coating thickness increases and evolves with aging processes [e.g., Riemer et al., 2010], the chemical and radiative properties of aged rBC particles can change dramatically compared to the ones of freshly emitted rBC [Schnaiter et al., 2005; Bond et al., 2006; Stier et al., 2007; Lack and Cappa, 2010]. However, the complex nature of both fresh and aged rBC particles makes it challenging to describe their microphysics (e.g., mixing state), chemical (e.g., composition of coating), and optical (e.g., influence of coating on the magnitude of rBC absorption) properties. Recent studies have highlighted that the morphology of rBC-containing particles is likely very different than the “core-shell” structure that is

typically assumed in many radiative models, and that rBC is not commonly located at the center but rather at the edge of an aerosol particle [Adachi *et al.*, 2010; Sedlacek *et al.*, 2012, and references therein]. Such irregular morphologies may be the reason (or one of the reasons) for the smaller-than-predicted absorption enhancements recently observed for atmospheric rBC-containing particles in an urban environment [Cappa *et al.*, 2012, and references therein]. Thus, there are still significant challenges related to understanding rBC properties and its effects on climate, as highlighted in a recent comprehensive review paper by Bond *et al.* [2013].

Extensive measurements of rBC mass loadings in different environments have taken place in the last two decades mainly by means of filter-based methods [Metcalf *et al.*, 2012, and references therein], which are relatively straightforward but do not provide information regarding the mass of the coating materials specifically associated with rBC particles. The introduction of the Single Particle Soot Photometer, SP2 [Stephens *et al.*, 2003], developed by Droplet Measurement Technologies (DMT), has represented a step forward in the characterization of rBC-containing particles, as the SP2 instrument allows for a real-time, sensitive quantification of rBC mass loadings and rBC-core size distributions on a single particle basis [Stephens *et al.*, 2003; Baumgardner *et al.*, 2004; Schwarz *et al.*, 2006]. The SP2 also provides methods for estimating the thickness of the coating material associated with an rBC core and the degree of mixing between core and coatings [e.g., Gao *et al.*, 2007; Schwarz *et al.*, 2008a, 2008b; McMeeking *et al.*, 2010; Subramanian *et al.*, 2010; Metcalf *et al.*, 2012]. However, the SP2 does not provide means to chemically speciate the coatings on rBC particles and is reliant on inversion methods to estimate the coating thickness. The Soot Particle Aerosol Mass Spectrometer (SP-AMS), recently developed by Aerodyne Research Inc. (ARI) [Onasch *et al.*, 2012], combines technologies from the DMT SP2 and the ARI high-resolution aerosol mass spectrometer (HR-AMS) [DeCarlo *et al.*, 2006] to provide real-time and quantitative information on the mass loadings and size-resolved chemical composition of rBC-containing particles, i.e., rBC and associated nonrefractory coating species.

Detailed measurements of the mass, size, chemical composition, and optical properties of rBC-containing particles were made as part of the California Research at the Nexus of Air Quality and Climate Change (CalNex) study on board the R/V *Atlantis* in early summer 2010 (starting in San Diego on 14 May 2010 and ending in San Francisco on 8 June 2010). The CalNex 2010 effort aimed to better quantify pollutant emissions and understand key atmospheric chemistry issues related to both air quality and climate change in California [Ryerson *et al.*, 2013]. The megacity of Los Angeles (LA) has been historically characterized by air quality problems and severe pollution episodes due to a constantly growing number of pollutant sources combined with unique meteorological and geographic features that often favor pollution stagnation [Lu and Turco, 1996; Angevine *et al.*, 2012]. Despite significant improvements due to the state's efforts in reducing pollutant emissions, high levels of particulate matter (PM) are consistently recorded in the LA basin (www.arb.ca.gov/html/brochure/history). Many recent field campaigns have shown that the majority of PM in the LA Basin is nowadays represented by organic aerosols, OA [Hayes *et al.*, 2013]; however, rBC emissions and concentrations in the LA area are still significant [Metcalf *et al.*, 2012].

As part of CalNex 2010, the R/V *Atlantis* was deployed to characterize air masses sampled along the California coast and to assess emissions from specific sources, e.g., ships in urban ports [Buffaloe *et al.*, 2014]. In addition to the R/V *Atlantis*, the study included two ground-based supersites (one at the California Institute of Technology campus in Pasadena and one near Bakersfield, in the San Joaquin Valley) and multiple research aircraft [Ryerson *et al.*, 2013]. On board the R/V *Atlantis*, we deployed a suite of particle instruments to investigate the chemical composition, volatility, hygroscopicity, and optical properties of the submicron aerosol, as well as changes in size, mass, and chemical composition of rBC-containing particles as a function of atmospheric aging. The implications of aging on the optical properties of rBC-containing particles (i.e., effects on absorption enhancement due to rBC particle coatings) have been discussed in Cappa *et al.* [2012]. Here we focus on the chemical and physical measurements obtained using the SP-AMS instrument and describe the size and mass spectral differences of the various types of air masses encountered during the deployment. We present cases of coastal pollution events as the R/V *Atlantis* often sampled air masses as they moved offshore from the LA basin. In addition, the particulate volatilities of these aerosols are explored with the ARI thermal denuder (TD). We also discuss the results of positive matrix factorization (PMF) analyses of the SP-AMS data and compare these results with PMF performed on the data from a standard colocated HR-AMS.

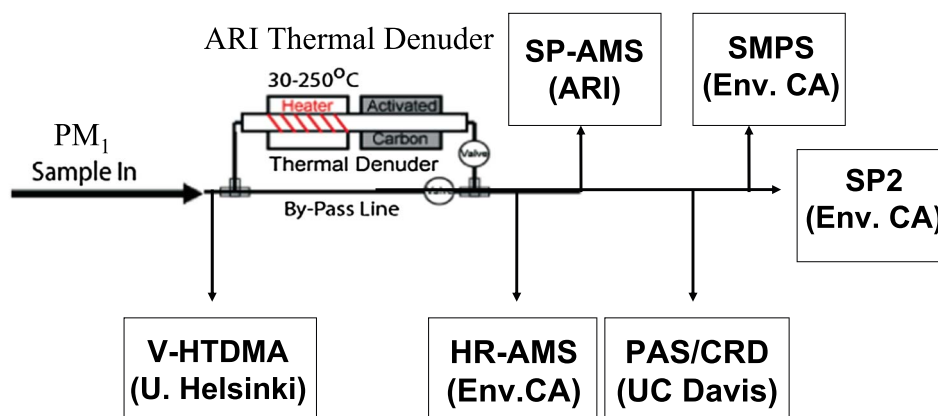


Figure 1. Schematic of the instrument setup described in this paper during the CalNex 2010 deployment (15 May to 8 June 2010) on the *R/V Atlantis*.

2. Methods

2.1. Aerosol Sampling and Instrument Setup

The aerosol sampling system on the *R/V Atlantis* during CalNex 2010 consisted of a 6 m long mast located 18 m above the ocean surface and pointing forward of the ship's stack. Periods of self-sampling were eliminated based on the wind direction and wind speed data measured relative to the position of the inlet (a more complete description of the mast can be found in *Bates et al.* [2012]). During CalNex 2010, the sampling mast was maintained at a relative humidity (RH) of 60% by controlling the mast temperature, and particles were sent to a suite of instruments after passing through a PM_{10} impactor and an ARI thermal denuder, TD, that was similar in design and performance to that described by *Huffman et al.* [2008]. Note that only the mast was kept at constant RH, whereas the sampling lines delivering particles to the various instruments had no RH control. The temperature in the heated section of the ARI TD was ramped between 30°C and 250°C and back over a period of 90 min. The sample flow was alternated between the unheated ("bypass mode") and heated ("TD mode") sections every 2.5 min [*Cappa et al.*, 2012]. The instruments located after the ARI TD included a DMT SP2 to measure single particle rBC mass and size; the ARI SP-AMS to measure the bulk mass and chemical composition of both rBC and the coating associated with rBC (hereafter NR- PM_{BC}) and their size distribution in the aerodynamic diameter (d_{va}) range 50–700 nm [*Canagaratna et al.*, 2007, and references therein]; a collocated standard HR-AMS to measure the ensemble mass and chemical composition of the total nonrefractory PM_{10} (NR- PM_{10}) and its size distribution in the same d_{va} range, 50–700 nm; a Scanning Mobility Particle Sizer (SMPS, TSI Inc., Model 3936) to measure the aerosol size distribution in the mobility diameter (d_m) range 20–600 nm; and the UC Davis Cavity Ringdown and Photoacoustic Spectrometers (CRD/PAS) to measure particle optical properties (light absorption and extinction) as a function of RH [*Langridge et al.*, 2011; *Lack et al.*, 2012]. The University of Helsinki Volatility Hygroscopicity Tandem Differential Mobility Analyzer (V-HTDMA) [*Villani et al.*, 2008], deployed to measure the hygroscopic growth factors (GF) as a function of particle size, volatility, and RH, sampled from the same PM_{10} line but operated its own TD. A schematic of the measurement setup on the *R/V Atlantis* is given in Figure 1. Additional details on each of these instruments are provided in *Cappa et al.* [2012].

2.2. SP-AMS and HR-AMS Measurements

The mass loadings and chemically resolved size distribution of rBC-containing particles were directly measured via the ARI SP-AMS. The instrument operating principles are discussed in *Onasch et al.* [2012]. The main feature of the SP-AMS is a 1064 nm continuous wave intracavity laser (similar in design to the SP2 laser) that is inserted into an HR-AMS chamber perpendicular to the particle beam axis. The laser vaporizes absorbing rBC at the aerosol sublimation/incandescence temperatures (~4000 K). In the SP-AMS, particles are first aerodynamically focused into the laser beam. As rBC-containing particles are heated by laser absorption, the coating material associated with rBC is vaporized, generating neutral chemical species. The removal of the coating allows the rBC core to heat up further and vaporize into neutral carbon clusters. The resulting

molecular vapor is ionized via 70 eV electron impact, and subsequent ion detection and chemical characterization occur via standard high-resolution mass spectrometry [Canagaratna *et al.*, 2007]. The SP-AMS measures the chemical composition and size distribution of both rBC and associated coating, NR-PM_{BC}, in the submicron range (note that the size distribution is representative of the total particle, rBC plus NR-PM_{BC}). We use the term NR-PM_{BC} to indicate the total coating material measured by the SP-AMS—organics (ORG), sulfate (SO₄²⁻), nitrate (NO₃⁻), ammonium (NH₄⁺), and chloride (Cl⁻)—which may include components that by definition are both nonrefractory and refractory, i.e., that vaporize in the laser below and above 600°C, respectively. In fact, the higher temperature attained by laser heating extends the range of detectable coating material associated with rBC [Corbin *et al.*, 2014].

The SP-AMS was calibrated for rBC quantification by determining the mass specific ionization efficiency (mIE_{BC}), or instrument sensitivity, for size-selected Regal Black particles [Onasch *et al.*, 2012]. The mIE_{BC} during CalNex 2010 was ~ 288 ions/pg. The 3σ detection limit for rBC was $<0.1 \mu\text{g m}^{-3}$ for 60 s averaging. In the SP-AMS, the collection efficiency (CE) for sampled particles, including the rBC and NR-PM_{BC} components, depends on the extent of overlap between the particle beam and the laser beam. If the ambient particle beam diverges more than the laser beam, the CE will be less than unity. Therefore, in the case of the SP-AMS, the CE depends primarily on the fraction of particles crossing the laser, and $CE < 1$ is likely due to losses of small and nonspherical particles in the SP-AMS because of particle beam divergence [Onasch *et al.*, 2012]. Recent work by Willis *et al.* [2014] suggests that the CE due to particle beam-laser beam overlap is similar for both rBC and NR-PM_{BC} components (i.e., the same CE should be applied for all rBC-containing particle chemical components). Willis *et al.* [2014] also note that the CE is dependent on the NR-PM_{BC}/rBC (coating to core) ratio, or R_{BC} , where a larger CE is expected for more coated (larger and more spherical) particles, which can focus more efficiently in the laser beam. Following Willis *et al.* [2014], we derived an R_{BC} -dependent CE correction for the SP-AMS data set (see Figure S1 of supporting information and related Text S2). During CalNex 2010, the CE was ~ 0.6 on average but varied from ~ 0.2 to 1.0 depending on the R_{BC} values. All the SP-AMS data reported in this paper are corrected using this derived R_{BC} -dependent CE.

The SP-AMS was operated in the laser-only configuration (i.e., without tungsten vaporizer) and in the V ion time of flight mode [DeCarlo *et al.*, 2006]. Note that in the laser-only configuration, the SP-AMS selectively and exclusively detects particles that absorb at 1064 nm, that is rBC, and its coating material NR-PM_{BC}. The data acquisition alternated between mass spectrum (MS) and particle time of flight (pToF) modes to obtain mass loadings and chemically resolved average size distributions.

The colocated HR-AMS provided the chemical composition and size distribution of NR-PM₁. The HR-AMS was operated in both V (high sensitivity, low mass resolution) and W (lower sensitivity, higher mass resolution) modes [DeCarlo *et al.*, 2006], but only the V mode data are used in this paper. The HR-AMS data were reported using a CE of 0.5 to account for particle bounce from the AMS vaporizer [Matthew *et al.*, 2008]. The CE was obtained against comparisons with SO₄²⁻ concentrations on filter samples analyzed by ion chromatography and checked against comparisons with a quadrupole AMS [Bates *et al.*, 2012]. Because the aerosol was dried enough and particle sulfate was neutralized, a particle phase-dependent CE correction [Middlebrook *et al.*, 2012] was not necessary. Both SP-AMS and HR-AMS data were analyzed using the high-resolution AMS data analysis software package PIKA [Sueper, 2010]. Positive matrix factorization (PMF) analyses were performed using the PMF2.exe algorithm (v.4.2) in robust mode [Paatero and Tapper, 1994]. The PMF inputs (mass spectral and error matrices) were prepared according to Zhang *et al.* [2011], and the solutions were evaluated with an Igor Pro based PMF Evaluation Tool (v. 2.04), following the method described by Ulbrich *et al.* [2009] and Zhang *et al.* [2011]. For both SP-AMS and HR-AMS data, the elemental analysis (EA) was performed using the recently updated oxygen-to-carbon (O/C) and hydrogen-to-carbon (H/C) ratios parameterization by Canagaratna *et al.* [2015a], which indicated that the standard analysis code of Aiken *et al.* [2007] can underestimate O/C and H/C by up to 30% and 10% respectively, especially for aerosol containing alcohol functional groups and dicarboxylic acids. All the data reported here are averaged to 10 min and do not include contributions from direct shipping emissions that are published elsewhere [Cappa *et al.*, 2014; Buffaloe *et al.*, 2014].

For the HR-AMS, the instrument uncertainty for the data reported in this paper is estimated to be +35/−15%. For the SP-AMS, the uncertainty in the mIE_{BC} calibration (i.e., rBC mass loading measurement) is approximately $\pm 20\%$, based on the uncertainties in size selecting a single-sized mobility diameter with known mass, and

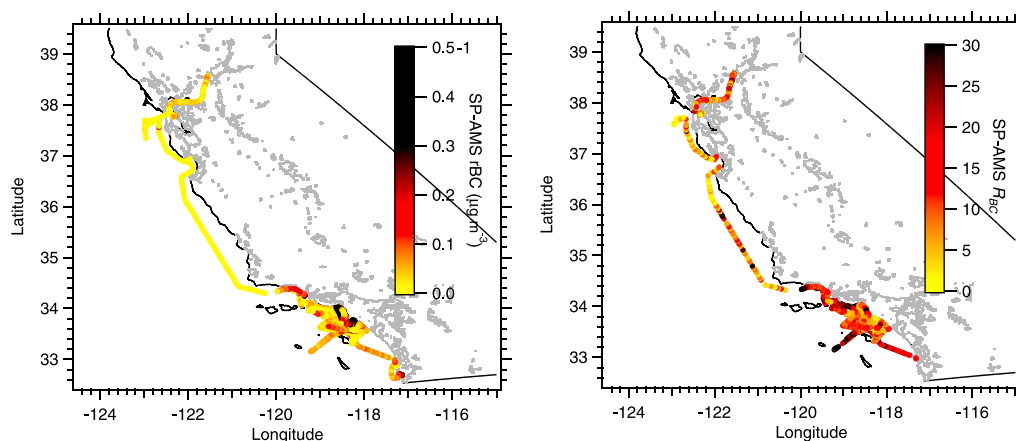


Figure 2. (left) SP-AMS rBC loadings (in $\mu\text{g m}^{-3}$) plotted along the R/V *Atlantis* cruise track. The highest rBC loadings were recorded nearby the Long Beach port areas. (right) SP-AMS R_{BC} (defined as $\text{NR-PM}_{\text{BC}}/\text{rBC}$) plotted along the cruise track. All data are averaged to 10 min.

counting the number concentration with a condensation particle counter. The uncertainty in the $mIE_{\text{NR-PM}_{\text{BC}}}$ calibration, estimated from mIE_{BC} and the relative ionization efficiency of rBC, RIE_{BC} [Onasch *et al.* [2012]], is approximately $\pm 50\%$. The SP-AMS R_{BC} -dependent CE correction is based on a direct comparison with the colocated SP2 instrument, which has an estimated uncertainty of $+100/-20\%$. Assuming that propagation of errors via addition in quadrature provides a useful error model, the combined mIE_{BC} and CE uncertainties suggest that the SP-AMS uncertainties are $+100/-30\%$ for rBC and $+112/-54\%$ for NR-PM_{BC} . These large uncertainties in the SP-AMS measurements are driven by the large SP2 uncertainties, which were unusually high for this study because of the instrument laser being misaligned (see full discussion in Text S1 of the supporting information). For both SP2 and SP-AMS, however, the precision is significantly higher than their corresponding absolute accuracies reported here.

3. Results and Discussion

3.1. Overview of the SP-AMS Measurements

The R/V *Atlantis* cruise track is shown in Figure 2, color coded by the SP-AMS rBC mass loadings (left) and R_{BC} (right). The campaign-average rBC mass loading was $0.3 \mu\text{g m}^{-3}$, with generally higher values measured in Southern California than in Northern California. The highest rBC loadings were recorded downwind of the LA basin, in particular in the port area of Long Beach ($\sim 1 \mu\text{g m}^{-3}$) and during periods when the R/V *Atlantis* sampled air masses coming from the LA urban area (rBC $\sim 0.5 \mu\text{g m}^{-3}$). Much lower rBC loadings ($< 0.1 \mu\text{g m}^{-3}$) were measured further away from the coast and/or when the air masses were influenced by clean marine air such as during the transit from Southern to Northern California. Typical rBC loadings measured in various Northern California locations (San Francisco Bay and Sacramento River) ranged from 0.1 to $0.25 \mu\text{g m}^{-3}$. Similar to rBC, the largest R_{BC} values were recorded in Southern California (up to 25) but varied greatly with location with a campaign-average value around 10.

Figure 3 shows the high-resolution time series of both rBC and its coating species (ORG, SO_4^{2-} , NO_3^- , NH_4^+ , and Chl^-) measured by the SP-AMS. The campaign-average pie chart shows that the majority of the NR-PM_{BC} material associated with rBC was represented by ORG, followed by SO_4^{2-} . The mass loadings of NR-PM_{BC} were generally enhanced when sampling air masses coming from the urban LA area, which also coincide with periods of high optical extinction and absorption levels observed by the CRD/PAS system [Cappa *et al.*, 2012]. These time periods are highlighted in Figure 3 and listed in Table 1. The three time periods highlighted by the solid boxes (labeled 1, 6, and 7) are chosen as case studies and will be discussed in section 3.2.

Figure 3 (bottom) also shows the SP-AMS chemically resolved average particle time of flight (pToF) size distributions ($dM/d\log_{10}d_{va}$) of rBC and coating species for Southern and Northern California. Similar to Massoli *et al.* [2012], we use the pToF of m/z 36 from unit mass resolution (UMR) data as a proxy for the rBC size distribution because the C_3^+ at m/z 36 is the strongest carbon signal and has relatively low interference

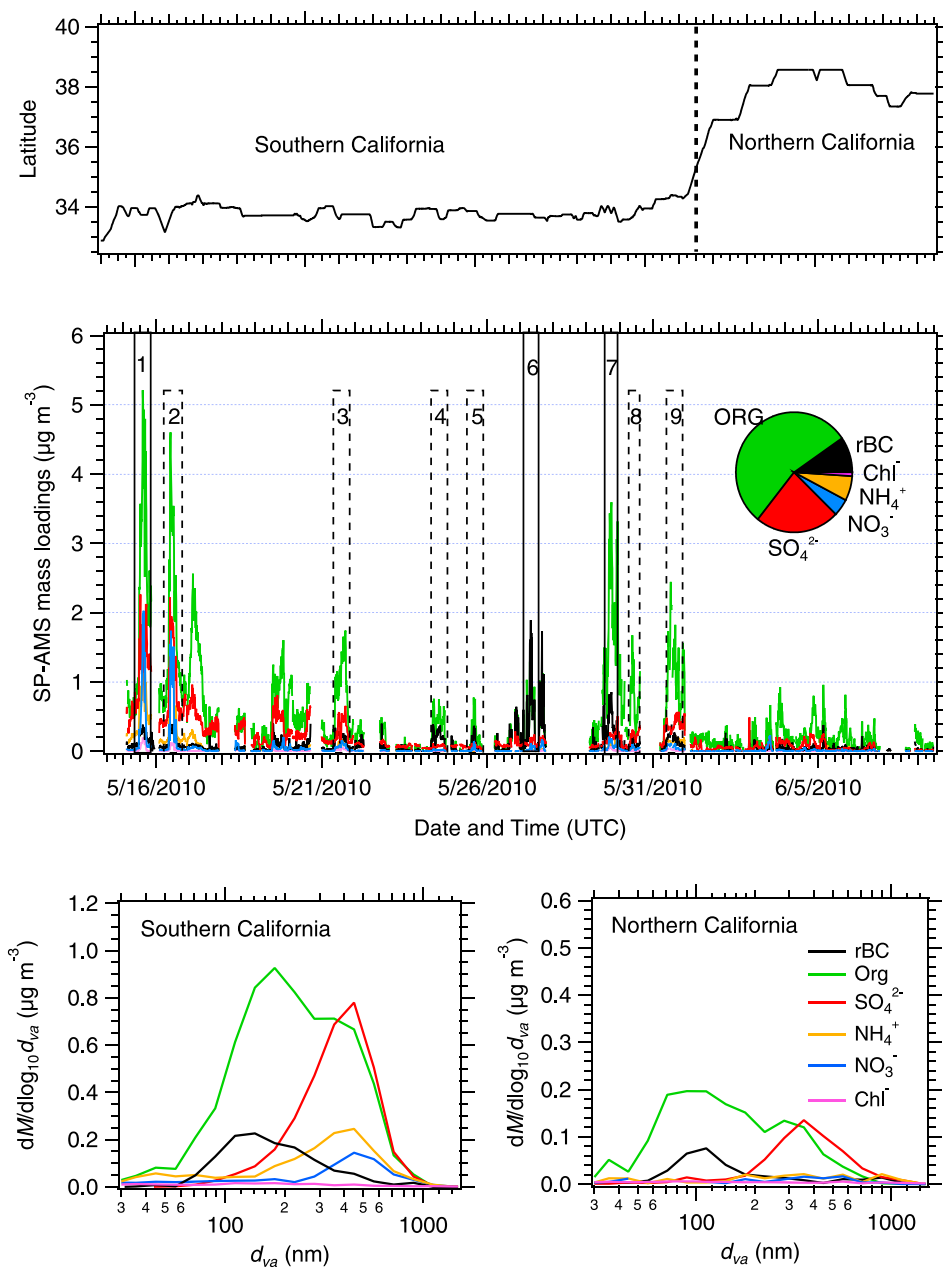


Figure 3. (top) Location (latitude versus time) of the R/V *Atlantis* during CalNex 2010. (middle) Temporal series of rBC and NR-PM_{BC} species (ORG, SO_4^{2-} , NO_3^- , NH_4^+ , and Chl^-) mass loadings measured by the SP-AMS. The sections highlighted in the solid boxes (labeled 1, 6, and 7) indicate the case studies described in section 3.2. The other dashed boxes highlight other LA outflow events sampled in the Santa Monica Bay (see Table 1). (bottom) SP-AMS chemically resolved average pToF size distributions ($dM/d\log_{10}d_{va}$) of rBC and NR-PM_{BC} species for Southern and Northern California.

from other particle components (Chl^- in this case). Still, the rBC size distribution traces reported here are corrected for the Chl^- signal. The Chl^- contribution to the m/z 36 pToF size distribution is estimated from HChl_{37} —the isotope of HChl_{35} at m/z 38, where all the pToF signal is attributable to HChl_{37} . After subtracting the estimated Chl^- (i.e., the HChl_{37} pToF trace multiplied by 3 to account for the isotopic ratio) from the total m/z 36, we obtain a rBC pToF trace, and then we scale the integrated area to the rBC mass concentration calculated from the high-resolution analysis, so that the rBC size distributions are quantitatively correct.

The pToF size distributions in Figure 3 show that, in general, most of the rBC mass is centered around ~ 100 – 120 nm d_{va} ; in the case of Southern California, however, the pToF size distribution of rBC extends

Table 1. List of Air Masses Sampled by the R/V Atlantis Off the Coast of Southern California, Mainly in the Santa Monica Bay, During the CalNex 2010 Research Cruise^a

| Date, Time (UTC) | Sampling Location (Air Mass Type) | R_{BC} (SP-AMS) | O/C (HR-AMS) | PCA |
|----------------------|---|-------------------|--------------|-------|
| 1) 15 May, 1130–1700 | Santa Monica Bay (nighttime chemistry) | 23 | 0.52 | 0.3 |
| 2) 16 May, 0930–1500 | Santa Monica Bay (nighttime chemistry) | 24 | 0.64 | 0.32 |
| 3) 21 May, 0930–1900 | Santa Monica Bay (nighttime chemistry) | 9 | 0.60 | 0.18 |
| 4) 24 May, 0800–1700 | Santa Monica Bay (offshore LAX) | 2.5 | n/a | 0.05 |
| 5) 25 May, 1230–1530 | Santa Monica Bay (offshore LAX) | 2.8 | 0.44 | 0.045 |
| 6) 27 May, 0430–1100 | Long Beach Port (fresh emissions) | 3 | 0.35 | 0.03 |
| 7) 29 May, 1500–2100 | Santa Monica Bay (daytime chemistry) | 6.1 | 0.43 | 0.05 |
| 8) 30 May, 0800–1130 | Offshore Palos Verdes (nighttime chemistry) | 10 | 0.66 | 0.45 |
| 9) 31 May, 1030–2000 | Offshore Ventura (nighttime chemistry) | 10.8 | 0.69 | 0.43 |

^aThe cases highlighted in gray (1, 6, and 7) are discussed in detail in the paper. The R_{BC} ratio (from the SP-AMS), the O/C ratio (from the HR-AMS), and the proxy for photochemical age PCA ($-\log([\text{NO}_x]/[\text{NO}_y])$), are reported for each event.

beyond 200 nm d_{va} , and rBC is present up to 500–600 nm $d_{va,r}$, indicating more compact rBC-containing particles at these larger sizes. As for the coating species, ORG is present across the all size range in both cases (although centered around 150 nm d_{va} in the Southern California case and ~ 100 nm d_{va} in the Northern California case, thus very similar to the ~ 100 nm d_{va} rBC mode), while SO_4^{2-} , NO_3^- , and NH_4^+ are almost exclusively above 200 nm d_{va} and peak at ~ 400 nm d_{va} . Cl^- was very low across the all d_{va} range throughout the CalNex campaign.

3.2. Measurements of Urban Air Masses in Santa Monica Bay

The R/V *Atlantis* spent a large fraction of the CalNex deployment (15–31 May 2010) in the Santa Monica Bay to sample air masses moving offshore from the LA urban area under the land/sea breeze regime. Several pollution studies conducted in the LA area in the last two decades have described in detail the meteorological phenomena that occur in the Southern California Bight such as the Catalina eddy [Angevine *et al.*, 2013, and references therein], often coupled with a local land/sea breeze circulation that is characterized by a very weak nighttime land breeze especially in the summer months [Lu and Turco, 1996]. Polluted air transported from the LA urban core toward the ocean by the nighttime land breeze (hereafter “LA outflows”) was sampled often by the R/V *Atlantis* in various locations within the Santa Monica Bay, typically under conditions of easterly-north easterly (E-NE), light winds ($< 2 \text{ m s}^{-1}$) [Wagner *et al.*, 2012]. It is worth noting that these air masses represent a multitude of emission sources that occur in the LA urban area mainly during the day and are pushed inland by the daytime sea breeze and then offshore by the nighttime land breeze (sometimes multiple times if rain or strong winds are absent for a few consecutive days). As a result, these air masses were processed by the time that they were measured by the R/V *Atlantis* located in the Santa Monica Bay. The outflow events (cf. Table 1) generally lasted 5–8 h each and were characterized by enhanced rBC (up to $0.5\text{--}1 \mu\text{g m}^{-3}$) and enhanced ORG in the SP-AMS NR-PM_{BC} and ORG and SO_4^{2-} in the HR-AMS NR-PM₁. In some outflows, enhanced NO_3^- was also observed in the SP-AMS NR-PM_{BC} (see Figure 3, middle). From the gas phase standpoint, the LA urban outflows were characterized by increased CO, NO, and NO_2 , and decreased O_3 [Wagner *et al.*, 2012, and references therein]. The mixing ratios of many volatile organic compounds (VOCs) measured by proton transfer reaction time-of-flight mass spectrometry (PTR-ToF-MS) [de Gouw and Warneke, 2007], i.e., acetaldehyde, acetone, formaldehyde, and aromatics (C_8 and C_9), were also slightly elevated in the outflows (see Figure S2 of supporting information). Table 1 reports key parameters for the LA outflow events, including estimates of photochemical age (PCA) obtained as ($-\log([\text{NO}_x]/[\text{NO}_y])$). As noted by Cappa *et al.* [2012], the dimensionless term ($-\log([\text{NO}_x]/[\text{NO}_y])$) is a proxy for photochemical age and serves as a “clock” under the assumption that the conversion of NO_x into NO_y occurs at a rate equal to $\text{NO}_2 + \text{OH}$ reaction rate. The PCA ranged from 0.05 to 0.45 for these outflow events, indicating fresh to moderately processed urban air masses, while the oxygen-to-carbon ratio (O/C) obtained from the HR-AMS ranged from 0.43 to 0.69, and R_{BC} ranged from 2.5 to 25. In general, O/C and R_{BC} increased with PCA—as one expects with aging—with the exception of the outflow cases of 15 May and 16 May, which had the highest R_{BC} among these case studies, but lower PCA than other outflow events with lower R_{BC} (e.g., 30 and 31 May). One possible explanation for this result is the sampling location: in fact, the sampling of 15 and 16 May occurred very close to the coastline in the Santa Monica Bay, whereas on 30 and 31 May the ship was further away from the coast and at the edges of the Santa Monica Bay

(offshore Palos Verdes and Ventura, respectively). Although it has been shown that the polluted urban air from LA carried by the land/sea breeze regime can reach well beyond the Santa Monica Bay [Wagner *et al.*, 2012, and references therein], differences in location and distance from the coastline—allowing mixing with more aged air masses—might have played a role, perhaps affecting PCA in a different manner than R_{BC} . The other—perhaps more likely—explanation is that 15 May (and 16 May) represented “special cases.” On 15 May—a Saturday—Metcalf *et al.* [2012] report aircraft measurements of a large increase of water soluble organic carbon relative to rBC (measured by an SP2) indicating SOA formation over the LA area, consistent with previous observations of SOA growth due to the so-called “weekend effect,” a phenomenon resulting from the lack of fresh emission—mostly from diesel engines—during the weekends [Metcalf *et al.*, 2012; Bahreini *et al.*, 2012]. However, a similar buildup of secondary material was not observed—at least at sea level—on the following weekend (21–22 May), when the LA outflow of 21 May exhibited lower PCA and R_{BC} than on 15 May. Interestingly, the meteorological data indicate rain on 18 and 19 May, which led to cleaner and perhaps less stagnant conditions in the following days.

In this section, we look more in detail at the chemical composition and average pToF size distribution of three distinct air masses sampled in different locations within the Santa Monica Bay (highlighted in Figure 3 as events 1, 6, and 7). Figure 4 shows the SP-AMS chemically resolved pToF size distributions and the high-resolution (HR) mass spectral profiles (MS) for the three case studies. The first case (Figures 4a and 4b) shows air masses sampled while the R/V *Atlantis* was in the Long Beach port area, thereby near direct emission sources. The second and the third cases are the outflows of 29 May 1500–2100 UTC (Figures 4c and 4d) and of 15 May 1130–1700 UTC (Figures 4e and 4f). In the pToF size distributions, the total ORG is split between the two main OA types identified by PMF analysis, i.e., hydrocarbon-like (HOA) and oxygenated organic aerosol (OOA) factors, which are, respectively, used as proxies for fresh and more aged aerosol [Zhang *et al.*, 2005a]. The HOA and OOA pToF traces are obtained using the tracer-based method described by Zhang *et al.* [2005a, 2005c], i.e., using, respectively, the UMR pToF size distributions at m/z 57 and m/z 44, and then scaling the integrated areas to the corresponding HOA and OOA mass loadings obtained by PMF analyses performed on the ORG matrix. The pie charts summarize the mass balance of the coating species.

The first case (#6 in Table 1 and Figure 3) is an example of fresh air masses sampled in the Long Beach port. The pToF trace (Figure 4a) shows that the rBC size distribution is centered around 100 nm d_{va} (“fresh soot mode”), and the pie chart indicates that rBC represents almost 50% of the total mass measured by the SP-AMS. Similar to rBC, ORG is found below 200 nm d_{va} , (although not completely internally mixed with rBC) and makes the majority of the measured NR-PM_{BC}; in this air mass, ORG is almost entirely made of HOA. Another small rBC mode peaking at 250 nm d_{va} (coated with HOA) is present. At larger d_{va} , there is additional rBC associated with small amounts of SO_4^{2-} , NO_3^- , and NH_4^+ (15% of the measured NR-PM_{BC}). In general, these pToF size distributions reveal a certain degree of external mixing between rBC and all of the NR-PM_{BC} species at both small and large d_{va} , consistent with relatively fresh emissions. The HR MS of rBC and ORG for this case study is shown in Figure 4b, with rBC represented by the ion family C_x^+ and ORG represented by ions of the $C_xH_y^+$, $C_xH_yO_1^+$, and $C_xH_yO_{>1}^+$ families. From the MS of the C_x^+ ions, we infer that most of the rBC signal (~90%) resides between C_1^+ ($m/z=12$) and C_5^+ ($m/z=60$), consistent with laboratory and previous ambient measurements [Onasch *et al.*, 2012; Massoli *et al.*, 2012; Corbin *et al.*, 2014] (see also Figure S3 of supporting information for examples of rBC MS for different soot types). The C_3^+ cluster ($m/z=36$) is the most abundant rBC peak, followed by C_1^+ ($m/z=12$) and C_2^+ ($m/z=24$). The MS is dominated by the characteristic $C_xH_{2y-1}^+$ and $C_xH_{2y+1}^+$ ion pattern of “HOA-like” aerosol, with the signals at $m/z=41$, $m/z=43$ ($C_3H_7^+$, the highest peak of the MS), $m/z=55$, and $m/z=57$ being the dominant peaks.

The case study of 29 May (#7 in Table 1 and Figure 3) is one of the outflow air masses sampled in the LA basin. The pToF plot (Figure 4c) shows that most of the rBC mass is centered around the $d_{va} \sim 100$ nm “fresh soot mode,” but a well defined rBC mode at ~ 400 nm d_{va} (“accumulation soot”) is also present. ORG makes about 90% of the total measured coating mass, and it is largely made of HOA, similar to the previous case. However, compared to the first case study, here rBC amounts to 23% of the total measured mass, and it is more heavily coated even at larger d_{va} , suggesting some degree of air mass processing. The corresponding HR MS of rBC and ORG is shown in Figure 4d. As in the previous case, most of the rBC signal (~90%) resides between C_1^+ ($m/z=12$) and C_5^+ ($m/z=60$), and the MS is largely dominated by the $C_xH_y^+$ ion type. However, here about 70% of the signal at $m/z=43$ (the most intense peak in the MS) is $C_2H_3O^+$.

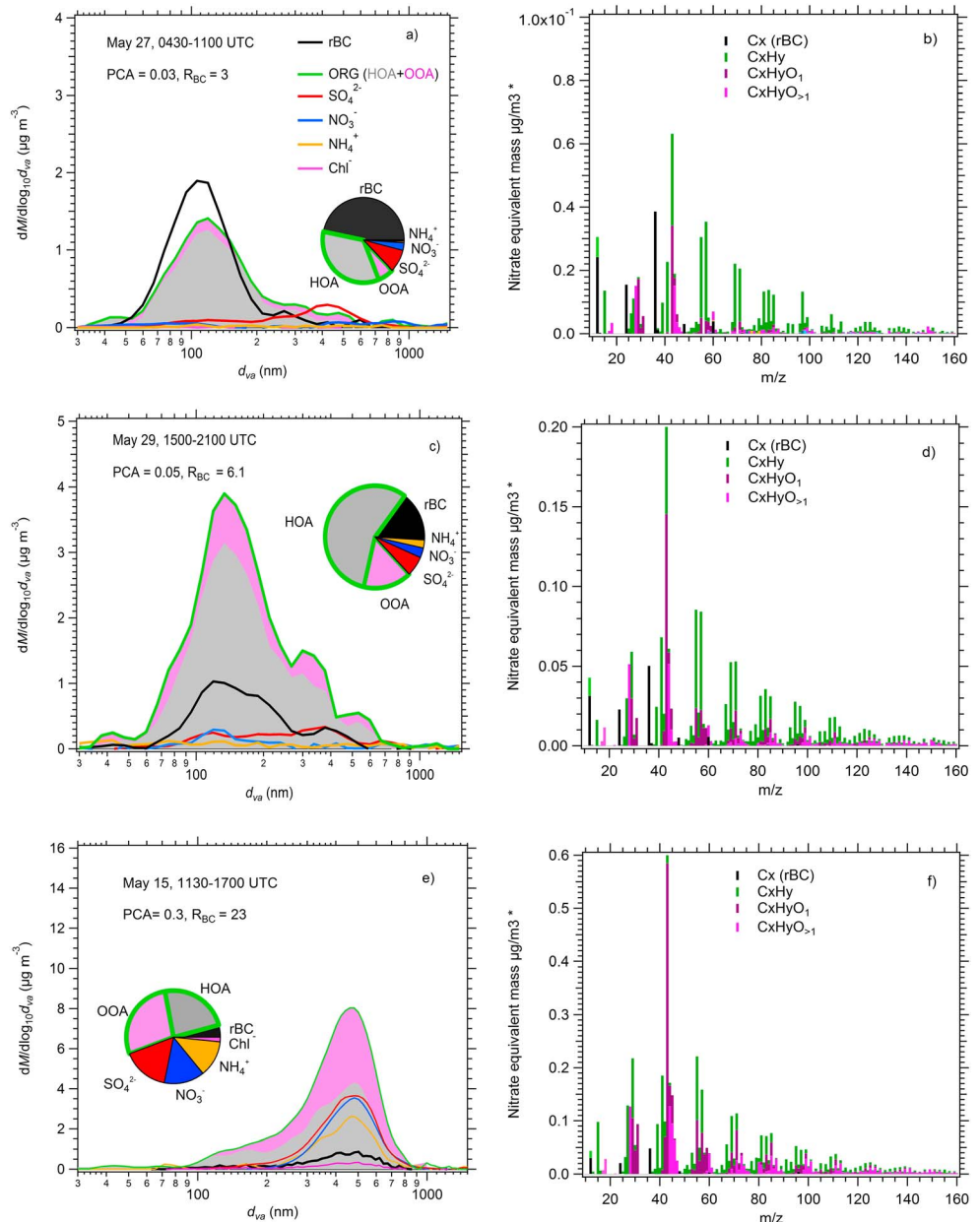


Figure 4. SP-AMS chemically resolved pToF size distributions ($dM/d\log_{10}d_{va}$), mass-weighted pie charts, and high-resolution mass spectral profiles (MS) of the ORG component for the three case studies of (a and b) 27 May, (c and d) 29 May, and (e and f) 15 May. The HOA and OOA contributions to the total ORG pToF traces are shown. The average PCA and SP-AMS-based R_{BC} are reported for all cases.

The third case (#1 in Table 1 and Figure 3) represents a more processed air mass during the outflow of 15 May. The pToF size distribution (Figure 4c) shows that the majority of both rBC and NR-PM_{BC} mass are shifted to larger d_{va} , ~450 nm. Refractory black carbon represents only 5% of the measured air mass, and it is coated by a much larger fraction of SO₄²⁻, NO₃⁻, NH₄⁺, and Chl⁻ compared to the previous outflow case. In addition, almost 50% of ORG is represented by OOA. Despite the two outflow case studies having different size distributions and different R_{BC} and PCA (larger values for 15 May, as discussed earlier), the difference in the MS is not as dramatic; however, oxygenated ions of the C_xH_yO₁⁺ and C_xH_yO_{>1}⁺ families are more abundant and make up a larger fraction of peaks such as $m/z = 41$, $m/z = 43$ (almost all C₂H₃O⁺), $m/z = 55$, $m/z = 71$, and $m/z = 85$.

The HR-AMS pToF size distributions and HR MS of the ORG component for the same three case studies are reported in Figure S4 of the supporting information. Generally, there is a good qualitative correspondence between SP-AMS and HR-AMS for the pToFs in the average peak of the ORG and SO_4^{2-} size distributions, even though the mass loadings are different and generally larger for the HR-AMS (particularly for the inorganic species in the accumulation mode regions, e.g., SO_4^{2-} , NO_3^- , and NH_4^+). One interesting observation is that in all the three cases, the HR-AMS MS are dominated by $m/z = 44$ (CO_2^+), whereas the MS of the SP-AMS are dominated by $m/z = 43$ (C_3H_7^+ and $\text{C}_2\text{H}_3\text{O}_1^+$). Laboratory studies suggest that the SP-AMS provides vaporization of the NR-PM_{BC} at lower temperatures compared to the standard tungsten vaporizer of the HR-AMS, resulting in less overall fragmentation and therefore less CO_2^+ production in the laser [Onasch *et al.*, 2012; Canagaratna *et al.*, 2015b]. The lower fragmentation also explains the larger presence of ion fragments above $m/z = 100$ in the SP-AMS spectra compared to the HR-AMS spectra.

3.3. PMF Analyses of SP-AMS and HR-AMS Data

PMF analyses of the SP-AMS CalNex 2010 data were performed on the ORG mass spectrum as well as on the combined mass spectral matrices of ORG and rBC (ORG + rBC) in order to extract information on the fraction and typology of ORG associated with rBC in different PMF factors. In this section, we discuss the results of the PMF performed on the ORG + rBC data and compare them to the PMF analysis of the HR-AMS ORG data. For the SP-AMS, we chose a four-factor solution with rotational forcing parameter $f_{\text{Peak}} = 0$ ($Q/Q_{\text{exp}} = 1.0$), yielding a hydrocarbon-like OA component, hereafter HOA + rBC, and three oxygenated OA components (OOA + rBC), two of which were recombined. The choice of a four-factor solution, as opposed to a three-factor solution, enabled the extraction of a more “standard” HOA MS (e.g., with $m/z = 44$ lower than $m/z = 43$ and $m/z = 43$ dominated by C_3H_7^+ rather than $\text{C}_2\text{H}_3\text{O}_1^+$). A detailed summary of key diagnostic plots of the PMF results and a discussion of the factor solution choices for the SP-AMS are reported in the supporting information (Figures S5–S8 and related text). For the HR-AMS, we also find that the data are best explained by a four-factor solution yielding an HOA and three OOA factors, two of which were recombined in a similar way to the SP-AMS data set.

Figure 5 presents the MS profiles and mass-weighted pie charts of the ion components for the three PMF factors HOA + rBC, SV-OOA + rBC (obtained by recombining two factors), and LV-OOA + rBC for the SP-AMS (a–c) and HOA, SV-OOA and LV-OOA for the HR-AMS (d–f). The H/C and O/C values of the PMF factors are also reported for both SP-AMS and HR-AMS. For the SP-AMS, the HOA + rBC factor (Figure 5a) is dominated by a characteristic $\text{C}_x\text{H}_{2y-1}^+$ and $\text{C}_x\text{H}_{2y+1}^+$ ion pattern, with the ions C_3H_7^+ ($m/z = 43$), C_4H_7^+ ($m/z = 55$), and C_4H_9^+ ($m/z = 57$) being the dominant C_xH_y^+ peaks. The rBC (represented by the ion family C_x^+) accounts for ~60% of the total HOA + rBC component mass concentration. The $\text{C}_x\text{H}_y\text{O}_1^+$ and the $\text{C}_x\text{H}_y\text{O}_{>1}^+$ ion families represent less than 20% of the total HOA + rBC mass. In the other two factors, rBC is about 15% of the total mass. SV-OOA + rBC (Figure 5b) is less oxygenated than LV-OOA + rBC (Figure 5c), which has the smallest fraction of C_xH_y^+ ions and the largest fraction of $\text{C}_x\text{H}_y\text{O}_{>1}^+$ ions among the three factors. The O/C and H/C values reported for the ORG component factors reflect this trend, with highest O/C and lowest H/C for the LV-OOA + rBC. Both SV- and LV-OOA + rBC show a small, yet significant, presence (~5% of the total mass) of $\text{C}_x\text{H}_y\text{O}_2\text{S}^+$ (organosulfates, mainly CH_3SO_2^+), $\text{C}_x\text{H}_y\text{N}_z^+$ (amines) and $\text{C}_x\text{H}_y\text{N}_z\text{O}_1^+$ (organonitrate) ions, which have been detected in previous HR-AMS data sets [Farmer *et al.*, 2010]. During CalNex 2010, N-containing ions were more abundant in the SV-OOA + rBC, while S-containing ions were only found in the LV-OOA + rBC factor. The same result applies to the HR-AMS.

Figure 5 shows that both SV-OOA + rBC and LV-OOA + rBC MS are dominated by the $\text{C}_2\text{H}_3\text{O}_1^+$ ion at $m/z = 43$, whereas the HR-AMS LV-OOA (Figure 5f) is dominated by CO_2^+ at $m/z = 44$, consistent with LV-OOA factors data from worldwide locations [Jimenez *et al.*, 2009; Ng *et al.*, 2010]. We already noted in the discussion of Figures 4 and S4 that this result is most likely related to differences in the fragmentation pattern of the SP-AMS compared to the standard HR-AMS because of the different vaporization scheme (laser versus tungsten vaporizer), as supported by the recent work of Canagaratna *et al.* [2015b]. To account for the differences in mass spectral fragmentation pattern, the SP-AMS H/C and O/C (calculated excluding rBC) are adjusted according to the SP-AMS-specific EA correction reported by Canagaratna *et al.* [2015b]. After this correction, the SP-AMS H/C values are 10–15% higher and the O/C values are 15–20% lower than the ones calculated for the HR-AMS factors.

Figure 6 shows the comparison between the SP-AMS and HR-AMS PMF factor time series (TS). The high correlation between the time series (r^2 values are 0.8, 0.85, and 0.70 for the HOA, SV-OOA, and LV-OOA factor

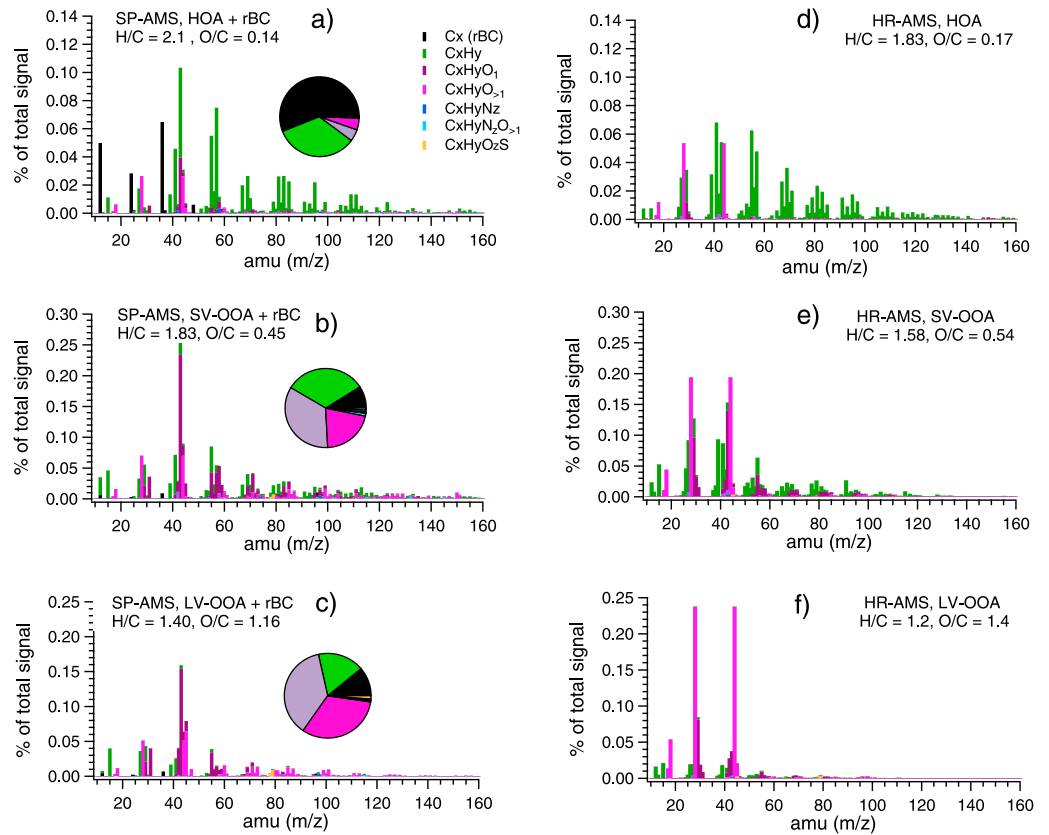


Figure 5. Results of the PMF analyses performed on the combined ORG + rBC matrices from the (a–c) SP-AMS and on the ORG matrix for the (d–f) HR-AMS. Mass-weighted pie charts of rBC and ORG ion families are shown for the SP-AMS HOA + rBC, SV-OOA + rBC, and LV-OOA + rBC factors. The HOA + rBC factor is dominated by C_xH_y , while the OOA factors have larger fractions of oxygenated ions. The O/C and H/C obtained with the new parameterizations by *Canagaratna et al.* [2015a, 2015b] are reported for both SP-AMS and HR-AMS.

pairs, respectively) indicates that the two instruments find virtually identical factor solutions. The high correlation between the HR-AMS PMF factors with ambient spectra from the high-resolution AMS database (see <http://cires.colorado.edu/jimenez-group/HRAMSsd> and *Ulbrich et al.* [2009]) supports this interpretation, with r^2 values of 0.98, 0.81, and 0.85 between our HR-AMS PMF factors and the database for the HOA, SV-OOA, and LV-OOA factors, respectively.

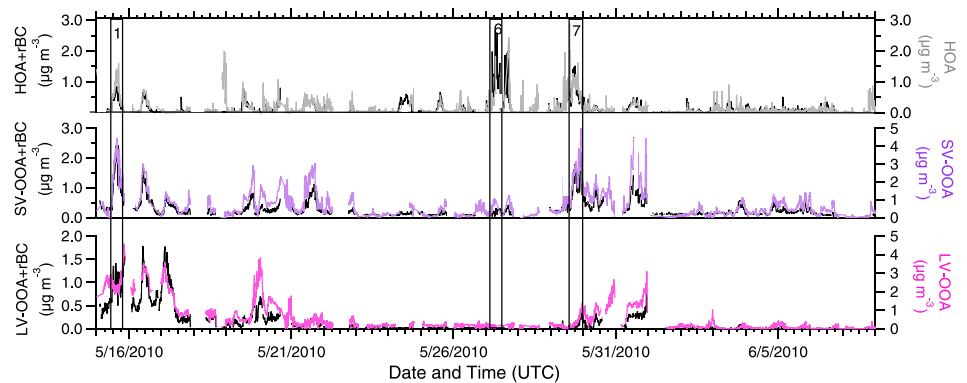


Figure 6. Time series illustrating the comparison between the SP-AMS (black traces) and HR-AMS PMF factors (color-coded traces). The comparison shows a good qualitative agreement, indicating that PMF finds similar solutions in both data sets. The r^2 between the PMF factors is 0.8 for HOA + rBC versus HOA, 0.85 for SV-OOA + rBC versus SV-OOA, and 0.7 for LV-OOA + rBC versus LV-OOA.

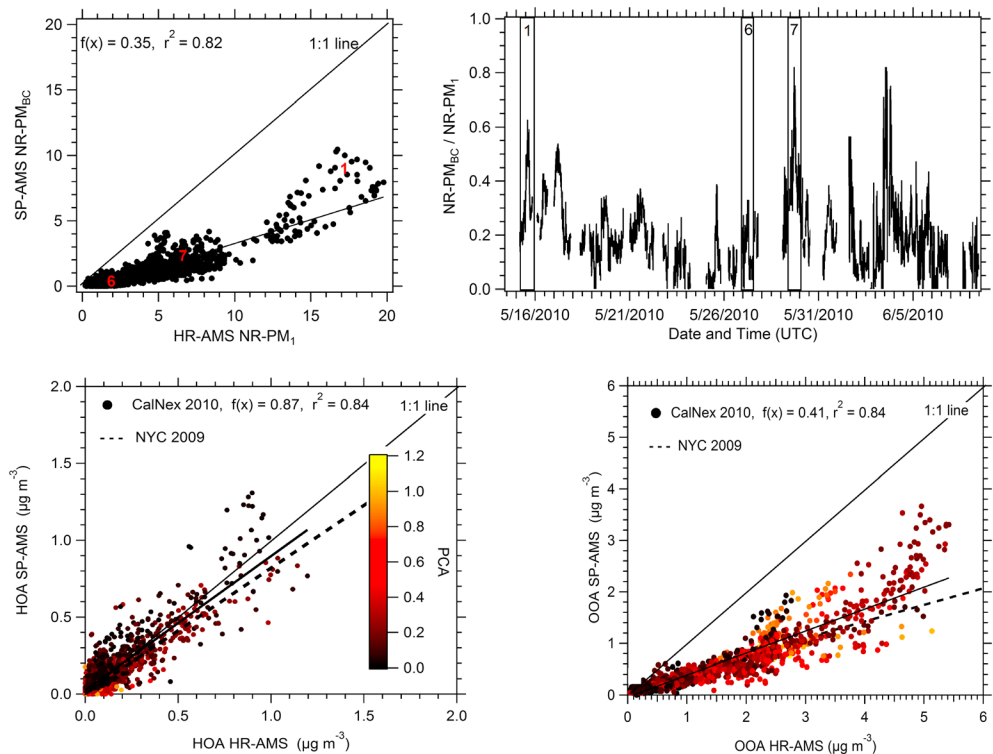


Figure 7. (top left) Correlation plot of SP-AMS NR-PM_{BC} versus HR-AMS NR-PM₁ and (top right) time series of the NR-PM_{BC} to NR-PM₁ ratio. The average mass fraction of the measured NR-PM₁ that is associated with rBC is 0.35. SP-AMS versus HR-AMS comparison for the (bottom left) HOA and (bottom right) OOA components, color coded by PCA. The fit to the CalNex data is shown by solid lines. The slopes of the correlation, $f(x)$, and the r^2 are also reported. The dashed lines indicate the fits to similar SP-AMS versus HR-AMS correlations from the NYC 2009 study [Massoli et al., 2012].

Figure 7 (top row) shows the comparison between ambient SP-AMS NR-PM_{BC} and ambient HR-AMS NR-PM₁, and the time series of the NR-PM_{BC}/NR-PM₁ (the fraction of NR-PM₁ associated with rBC) for the entire CalNex 2010 campaign. Figure also indicates the three case studies (1, 6, and 7) discussed previously. Based on the scatterplot (top left), the fraction of the NR-PM₁ mass measured by the HR-AMS that is associated with rBC is 35% on average, but it is greatly variable throughout the campaign (0.05 to 0.8) as shown by the time series of the NR-PM_{BC} to NR-PM₁ ratio (top right). Figure 7 (bottom row) instead shows the comparison between SP-AMS and HR-AMS PMF HOA (bottom left) and total OOA (bottom right), color coded by PCA. For this particular comparison, we use the results from the PMF analysis performed only on the ORG matrix of the SP-AMS data to allow a more direct comparison with the HR-AMS PMF solutions. It is worth noting that the PMF analysis performed on the SP-AMS ORG matrix yields virtually the same MS profiles and TS as obtained for the ORG + rBC matrix (see Figure S9 for the complete TS comparison of the SP-AMS and HR-AMS PMF factors with both PMF analyses performed on the ORG matrix). The HOA comparison in Figure 7 (bottom left) yields a regression slope—solid line—of 0.87 ($r^2 = 0.84$), suggesting that the ambient HOA during CalNex 2010 was almost entirely associated with rBC and, therefore, detected by the SP-AMS. The color coding indicates that the majority of HOA has PCA < 0.4, as expected due to the association of this factor with fresh air masses. For reference, we also show the best fit line from a similar comparison on SP-AMS and collocated HR-AMS data collected during the NYC 2009 study [Massoli et al., 2012] for which the HOA comparison gave a correlation slope of 0.81 (dashed line). In the OOA case, the correlation for CalNex yields a slope of 0.41 ($r^2 = 0.84$), indicating that 41% of the measured total OOA was associated with rBC; for comparison, this fraction was 35% during the NYC 2009 study.

Figure 8 shows further comparisons between the SP-AMS NR-PM_{BC} and HR-AMS NR-PM₁ for the inorganic species NO₃⁻, NH₄⁺, Cl⁻, and SO₄²⁻. The slopes (solid lines) are 0.6, 0.26, 0.51, and 0.21, respectively, and indicate the fraction of the NR-PM₁ that is detected by the SP-AMS as NR-PM_{BC}. The dashed lines represent the slopes obtained from the SP-AMS and HR-AMS comparison during the NYC 2009 study [Massoli et al., 2012].

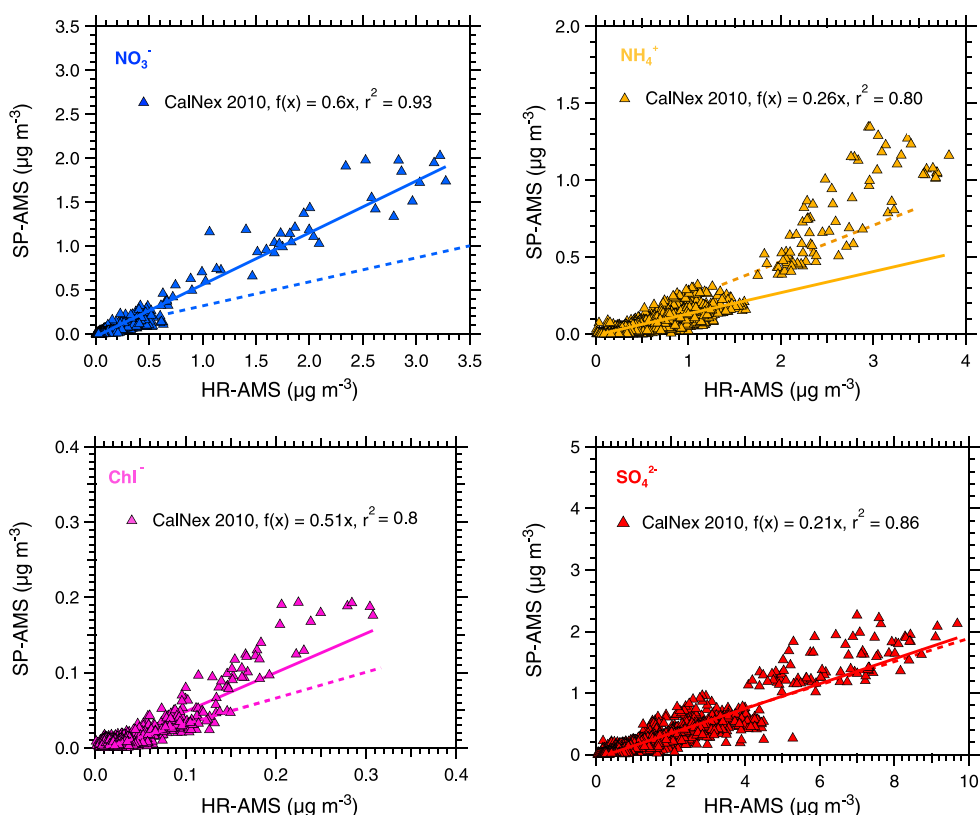


Figure 8. SP-AMS NR-PM_{BC} versus HR-AMS NR-PM₁ scatterplots of the SO_4^{2-} , NO_3^- , NH_4^+ , and Cl^- mass loadings ($\mu\text{g m}^{-3}$). The fits to the data are shown by the solid lines. The slopes of the correlation, $f(x)$, and the r^2 are also reported. The dashed lines indicate the fits to similar SP-AMS versus HR-AMS correlations from the NYC 2009 study.

It appears that, in both campaigns, SO_4^{2-} and NH_4^+ are the inorganic species least associated with rBC. The size distributions presented earlier show that these components are typically found in the accumulation mode soot, also consistent with previous results from typical HR-AMS ambient data [e.g., Zhang *et al.*, 2005b; Canagaratna *et al.*, 2007]. It has to be noted for these scatterplots that the data points above 0.5, 0.15, and $2 \mu\text{g m}^{-3}$ for the NH_4^+ , Cl^- , and SO_4^{2-} SP-AMS loadings, respectively, lie slightly above the campaign-average fit lines (the same is true for the OOA loadings above $3 \mu\text{g m}^{-3}$ in Figure 7 (bottom right)). These points correspond to the outflows of 15 and 16 May, which had a much larger R_{BC} than the rest of the data set. While there does appear to be a consistent, general trend in the measured NR-PM₁ mass fractions associated with rBC particles, it is not clear that these fractions need to remain constant under all conditions. Thus, the apparent variable slopes in the correlations may be due to different atmospheric conditions. It is also possible that the R_{BC} -dependent CE that we apply to the data, defined as an average correction curve to the data set (see Figure S1), may not capture—or correct for—the entire data variability. At the moment, this approach provides the best CE correction. In the future, SP-AMS measurements that also incorporate a direct measure of the changes in particle beam width with coating thickness using beam width probe measurements—as done by Willis *et al.* [2014]—may allow to directly measure the degree of particle to laser beam overlap (effectively the CE) and correct for differences in sensitivities with particle coating more accurately.

In order to further support our estimates of total NR-PM₁ associated with rBC, we tried to extract the same information by using other data independently acquired during the CalNex 2010 campaign, in particular, data from the V-HTDMA housed in the same container and data from an SMPS system housed in another container therefore sampling from a different inlet line, both operating downstream of their own TD. The V-HTDMA was set to measure three dry particle sizes, 50, 100, and 145 nm d_m . The hygroscopic growth factors, GF, were measured at 90% RH. The TD was set to ramp the temperature up and down from 50°C to 280°C in a 45 min interval, and the size distribution scan for each size occurred in 240 s with thermal denuder,

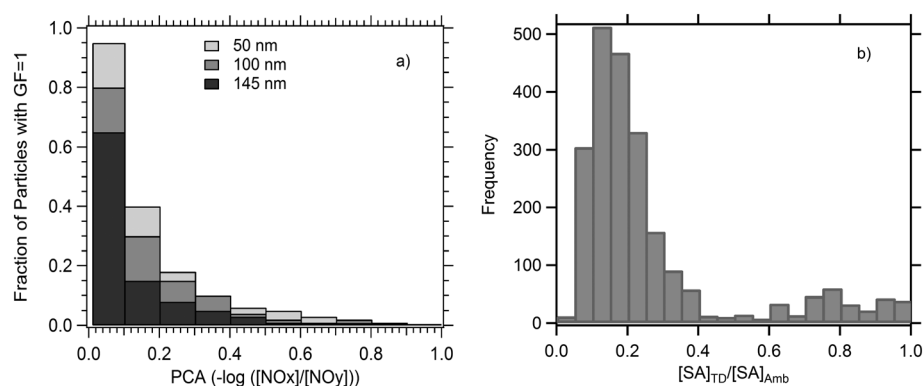


Figure 9. (a) V-HTDMA-based frequency distribution of the number fraction of particles with $GF = 1$ plotted as a function of the photochemical age proxy (PCA). Most of particles with $GF = 1$ have $PCA < 0.4$. (b) Frequency distribution of the SMPS-based TD/ambient surface area (SA). The average SA_{TD}/SA_{AMB} ratio is 0.30, corresponding to $\sim 30\%$ of PM_{10} mass associated with rBC.

and in 180 s without. The V-HTDMA measurements indicate that, on average, about 20% of the selected particles—by number—were hydrophobic ($GF = 1$), suggesting the presence of refractory material, e.g., rBC. When plotting the fraction of particles with $GF = 1$ as a function of PCA (Figure 9a), we observe that the vast majority of these particles fall in the region with $PCA < 0.4$, with very little variability related to the initial dry particle size. This result is consistent with the hydrophobic nature of freshly emitted rBC-containing particles.

The TD connected to the SMPS was operated at 230°C . The airstream was split into two flows (ambient and denuded), dried with nafion driers before the denuder, and then measured with two SMPSs. The TD was periodically operated at ambient temperature to measure and correct for any sampling biases from the two SMPSs. The SMPS study-averaged integrated volume, number and surface area concentrations for the ambient, and TD periods were used to calculate the ratio of the TD/ambient surface area (SA) concentrations. We obtained an average spherical particle surface area ratio SA_{TD}/SA_{AMB} distributed around 0.30, or 30% (Figure 9b), a median SA ratio of 0.18 and only a few data points with SA_{TD}/SA_{AMB} larger than 0.4. We note that thermally denuded SMPS SA ratio results may be biased high because of the spherical particle shape assumption and by the fact that the thermally denuded SMPS results may include other refractory material such as sea salt (although the sea salt fraction in PM_{10} is usually very small); we therefore estimate that 30% represents an upper limit for the condensable secondary NR- PM_{10} material that would be associated with rBC particles. Overall, these independently calculated numbers compare well with the measured fraction of particles containing rBC as obtained from the comparison of the SP-AMS and HR-AMS data, i.e., 35% as a campaign average (cf. Figure 7, top left).

3.4. Thermal Denuder Measurements

The combination of the TD with the SP-AMS measurements allowed to obtain chemically resolved volatility profiles of the sampled ambient particles through evaporation of the NR- PM_{10} material induced by heating. As described in detail by *Cappa et al.* [2012], the particles sampled through the TD enter a heating stage, then pass through a charcoal diffusion denuder stage to prevent recondensation of volatile gases. During CalNex 2010, the flow rate through the TD was 1.5 lpm, corresponding to a residence time in the entire heated section of 8.5 s. The temperature in the heated section of the TD was ramped from 30°C to $\sim 220^{\circ}\text{C}$ and back over a period of 90 min. The sample flow was alternated between the unheated (bypass mode) and heated (TD mode) sections every 2.5 min using two computer-controlled actuated stem valves. A small flow (0.3 lpm) always passed through the line that was not in use to allow the system to respond rapidly after switching between modes. Based on the principle that rBC does not evaporate in the TD, the rBC measurements made using the SP2 behind the TD allowed estimation of the rBC mass loss through the TD [*Huffman et al.*, 2008]. The average temperature dependent transmission function (Tr), defined as the ratio between the rBC mass after passing through the TD versus bypass line [*Cappa et al.*, 2012], was $Tr = 0.95 - 0.00083 \cdot T_{TD} (^{\circ}\text{C})$, which compares very well with that estimated by *Huffman et al.* [2008] for a typical distribution of ambient submicron particles. However, for this data set, rather than using the average T-dependent transmission function, the correction for particle losses was performed by normalizing the measured ambient and TD NR- PM_{10} data by the

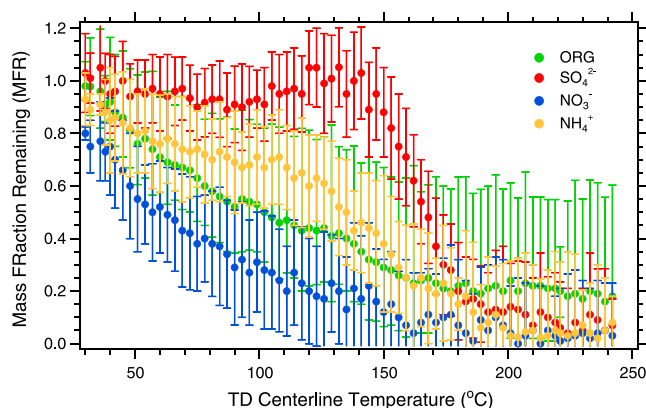


Figure 10. Volatility profiles (“thermograms”) for the SP-AMS NR-PMBC species ORG, SO_4^{2-} , NO_3^- , and NH_4^+ . The data are reported as mass fraction remaining (MFR) as function of the centerline thermal denuder (TD) temperature. The error bars represent the variability in the data (1σ standard deviation of the measurements).

corresponding rBC mass loadings—a point-by-point correction—in order to reduce the scatter in the resulting corrected data.

Figure 10 shows the average TD “thermogram” (i.e., the plot of the mass fraction remaining after heating as a function of TD temperature) for the SP-AMS coating species ORG, SO_4^{2-} , NO_3^- , and NH_4^+ for the entire campaign (the volatility profile of Cl^- is not shown because of the low signal to noise). The NO_3^- profile shows the highest volatility of all coating species, with the remaining mass fraction (MFR) below 0.2 already at $\sim 150^\circ\text{C}$. SO_4^{2-} is the least volatile component, with MFR > 0.8 up to 140°C , followed by a rapid MFR drop to 0.2 between 150° and 180°C . The initial decrease of the MFR SO_4^{2-} values between 50° and 100°C followed by an increase between 100° and 150°C is a feature that has been observed in previous ambient data and it has been attributed to physical changes in particle sulfate phase or morphology [Huffman *et al.*, 2008]. The ORG coating has intermediate volatility between SO_4^{2-} and NO_3^- , with a MFR value of 0.5 at 100°C ; however, the ORG MFR stays around MFR = 0.2 above 150°C , indicating that some of the ORG is much less volatile than, e.g., SO_4^{2-} and NO_3^- at those temperatures. Finally, the NH_4^+ thermogram shows lower volatility than ORG and NO_3^- at $T < 150^\circ\text{C}$, with a rapid drop afterward. Comparison with previous literature data [Huffman *et al.*, 2009; Docherty *et al.*, 2011] indicates that the SP-AMS NR-PMBC material evaporates similar to the total NR-PM₁. For temperatures above 200°C , at least 80% of NR-PMBC material is removed from the ambient rBC-containing particles.

As discussed in Cappa *et al.* [2012], significant charring can be excluded based on the fact that most of the NR-PMBC components are evaporated before high temperatures are reached; for $T > 200^\circ\text{C}$, the MFR values are < 0.2 and only a small fraction of the initial ORG ($< 5\%$) is potentially charred upon heating. Figure S10 shows the normalized, high-resolution SP-AMS mass spectra of rBC for the average ambient (top left) and for thermally denuded data with $T > 200^\circ\text{C}$ (top right). The distribution of the rBC C_n^+ ions and their relative intensities is overall similar, even if the abundances of C_2^+ , C_4^+ , and C_8^+ relative to C_3^+ differ (e.g., $\text{C}_2^+/\text{C}_3^+$ is higher in the ambient case). The campaign-average, chemically resolved pToF size distributions corresponding to ambient and thermal denuder conditions ($T > 200^\circ\text{C}$), is also shown (bottom row). The aforementioned small fractions of ORG and SO_4^{2-} that remain at elevated temperatures are observed in the accumulation mode of the thermally denuded pToF traces, consistent with Cappa *et al.* [2013].

Figure 11 shows the thermograms of the rBC coating species ORG, SO_4^{2-} , NO_3^- , NH_4^+ , and Cl^- (a and b), CO_2^+ (c and d) and other key ions (C_3H_7^+ , C_4H_9^+ , and $\text{C}_2\text{H}_3\text{O}^+$, e and f) for the case studies of 29 May and 15 May 2010, that represent examples of moderately aged and aged urban air masses, respectively (cf. Figure 4). The data from 27 May are not reported here because there were no thermal denuder data collected during those times. The thermograms of the coating species are similar in both cases, with the only exception for SO_4^{2-} which has a more pronounced increase at 140°C in the case of 15 May. Likewise, the volatility of the C_3H_7^+ , C_4H_9^+ , and $\text{C}_2\text{H}_3\text{O}^+$ ions (where $\text{C}_2\text{H}_3\text{O}^+$ is the most abundant fragment in both mass spectra of Figures 4d and 4f, respectively) is similar between the two cases. There is instead a striking difference in the trend of the CO_2^+ ion, which decreases with T for the 15 May case (where the fraction of CO_2^+ in the MS in Figure 4d, $f_{\text{CO}_2^+}$, is 0.05), but it remains almost flat in the case of 29 May (for which $f_{\text{CO}_2^+} = 0.126$, cf. Figure 4f). In the attempt to estimate the fraction of CO_2^+ that is refractory, we calculated a refractory CO_2^+ component (R- CO_2) using the correlation between the measured fragment CO_2^+ and rBC, allowing estimation of the fraction of particle CO_2^+ that is associated with rBC. The nonrefractory component (NR- CO_2) is then obtained by subtracting R- CO_2 from the measured CO_2^+ . In the case of 29 May (Figure 11c), the calculated NR- CO_2 fraction is virtually zero and the

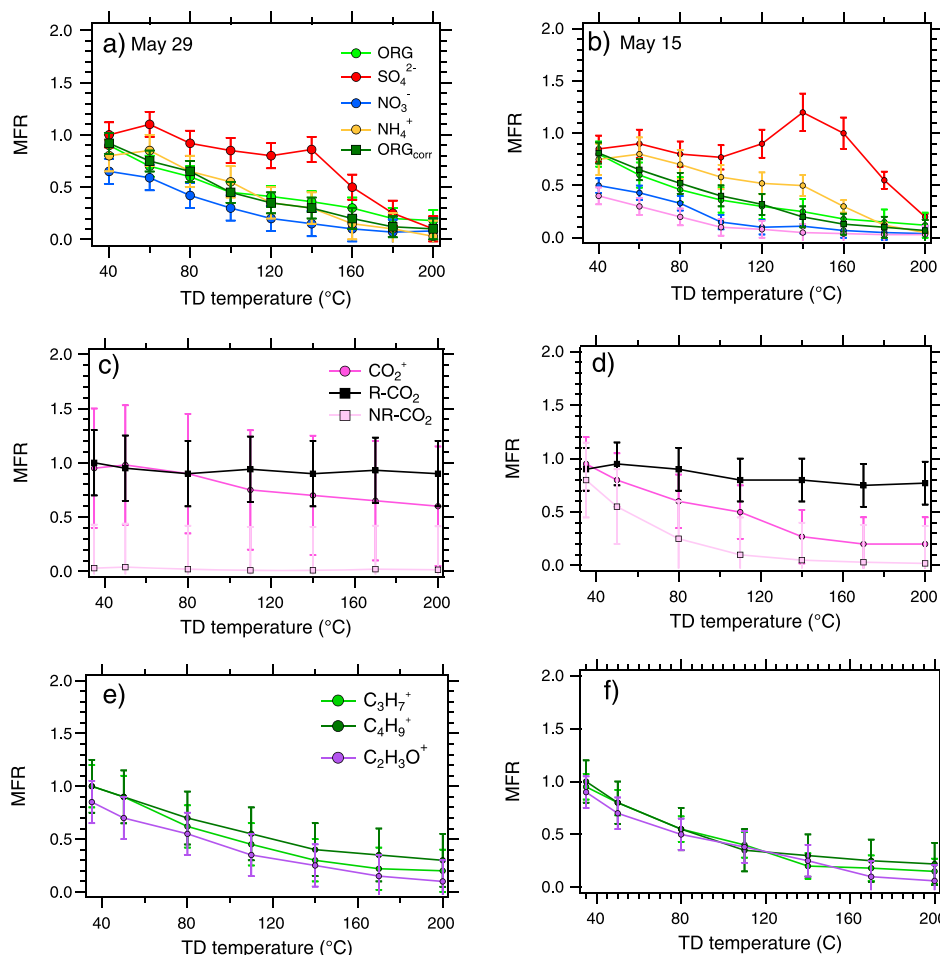


Figure 11. Thermograms of the SP-AMS NR-PM_{BC} species (a and b) ORG, SO₄²⁻, NO₃⁻, NH₄⁺, and Cl⁻, (c and d) CO₂⁺, and (e and f) C₃H₇⁺, C₄H₉⁺, and C₂H₃O⁺ for the case studies of 29 May (Figures 11a, 11c, and 11e) and 15 May (Figures 11b, 11d, and 11f). On 15 May, the CO₂⁺ ion has the “expected” volatility profile, whereas it remains almost flat in the case of 29 May, indicating the presence of refractory, nonvolatile organic coating material. The error bars represent the 1σ standard deviation of the measurements.

measured CO₂⁺ follows the trend of the calculated R-CO₂, whereas on 15 May (Figure 11d) the measured CO₂⁺ follows the trend of the calculated NR-CO₂. We interpret this result as an indication of the different nature (and volatility) of the CO₂⁺ fragment depending on the type of air mass and coating material that is associated with rBC. In the case of 29 May, an example of relatively fresh emissions with the majority of ORG coating represented by HOA, the CO₂⁺ fragment likely originates from refractory oxygen species that form during the oxidation of organic material on the rBC surface. The existence of a refractory CO₂⁺ fragment has been observed in the laboratory for certain types of soot (rBC) particles such as those generated using a propane diffusion flame [Onasch *et al.*, 2012; Corbin *et al.*, 2014]. In the case of 15 May, a more aged air mass with ~ 50% of ORG represented by OOA, the CO₂⁺ fragment follows the expected trend based on previous HR-AMS observations [Huffman *et al.*, 2009] and it is probably originated from oxidized organic material condensed onto preexisting rBC particles.

Finally, we estimate the fraction of ORG that is purely nonrefractory by subtracting the contribution of the estimated R-CO₂ fraction to the total measured ORG, which at 200°C has MFR values of 0.2 and 0.1 for 29 May and 15 May, respectively. The resulting ORG_{corr} (obtained as ORG minus R-CO₂) is shown in Figures 11a and 11b. In the case of 29 May, the MFR of ORG_{corr} drops below the MFR of ORG starting at $T > 120^{\circ}\text{C}$, and it is significantly lower (45%) than ORG MFR at 200°C. On 15 May, the MFR of ORG_{corr} is “only” 25% lower than ORG MFR at 200°C, consistent with the presence of less refractory organic material in this more aged air mass.

4. Summary and Conclusions

We present measurements of black carbon-containing particles made during the CalNex 2010 study on board the R/V *Atlantis* for the period 15 May to 8 June 2010. An ARI soot particle aerosol mass spectrometer (SP-AMS) provided detailed measurements of the size-resolved chemical composition of refractory black carbon (rBC) and the associated coating species. The peak in the average size distribution of the rBC as measured by the SP-AMS in vacuum aerodynamic diameter, d_{va} , varied from ~ 100 nm d_{va} (fresh rBC emissions) to ~ 450 nm d_{va} (accumulation mode rBC, typical of more processed rBC-containing air masses). In general, rBC was associated with an organic aerosol (ORG) coating. A colocated standard high-resolution aerosol mass spectrometer (HR-AMS) measured the nonrefractory portion of the submicron aerosol or NR-PM₁. The combination of the two instruments allows an estimate of the fraction of the NR-PM₁ that is associated with rBC (or NR-PM_{BC}, when referring to the SP-AMS). Our results indicate that, on average, 35% of the NR-PM₁ mass was associated with rBC, with some variability observed upon source and coating species. Detailed comparisons between the SP-AMS NR-PM_{BC} and HR-AMS NR-PM₁ revealed that the SP-AMS detected most of the primary NR-PM₁ (87% of the HOA) and 28% of the secondary NR-PM₁, as obtained from the mass-weighted average of all the remaining NR-PM_{BC} species. Consistently, positive matrix factorization (PMF) analyses of both NR-PM₁ and NR-PM_{BC} indicate that rBC is mostly associated with hydrocarbon-like organic aerosol (HOA). PMF results from SP-AMS and HR-AMS compare well, though differences in the fragmentation pattern due to the different vaporization techniques (laser versus tungsten vaporizer) can be observed. The use of the thermal denuder (TD) allowed investigation of the volatility of the coating material exclusively associated with rBC. The volatility properties of less oxidized masses indicate the presence of refractory organic material (detected as CO₂⁺) associated with rBC. Additional field measurements and laboratory experiments will be needed to improve our current understanding of the sources and properties of nonvolatile (refractory) oxygenated material associated with soot particles.

Acknowledgments

The authors thank the crew of the R/V *Atlantis*, and Derek Coffman and Drew Hamilton of NOAA PMEL for their assistance and help during the project. Thanks to Eric Williams and Brian Lerner (NOAA CSD) for sharing the CO, CO₂, NO_x, NO_y, and O₃ data, and to Alexander Vlashenko (Environment Canada) for sharing the VOC data. We thank Manjula Canagaratna and Leah Williams for their useful comments. This project was funded by the NOAA Global Climate Change Program (NA09AR4310125 and NA09OAR4310124), the California Air Resources Board, the National Center for Environmental Research (NCER) at USEPA (RD834558), the Canadian Federal Government (PERD Project C12.007), and NSERC. The SP-AMS instrument was developed with funding from the U.S. Department of Energy SBIR Program (DE-FG02-07ER8489009). This manuscript has not been reviewed by any of the funding agencies. The results shown in the paper will be provided to the readers. The SP-AMS data can be accessed via the data server of the Pacific Marine Environmental Laboratory, PMEL (<http://saga.pmel.noaa.gov/Field/CalNex/index.html>). Other data and, if necessary, the code used in obtaining the results presented here will be provided upon inquiring to the corresponding author (pmassoli@aerodyne.com).

References

- Adachi, K., S. H. Chung, and P. R. Buseck (2010), Shapes of soot aerosol particles and implications for their effects on climate, *J. Geophys. Res.*, **115**, D15206, doi:10.1029/2009JD012868.
- Aiken, A. C., P. F. DeCarlo, and J. L. Jimenez (2007), Elemental analysis of organic species with electron ionization high-resolution mass spectrometry, *Anal. Chem.*, **79**, 8350–8358, doi:10.1021/ac071150w.
- Angevine, W. M., L. Eddington, K. Durkee, C. Fairall, L. Bianco, and J. Brioude (2012), Meteorological model evaluation for CalNex 2010, *Mon. Weather Rev.*, **140**(12), 3885–3906, doi:10.1175/MWR-D-12-00042.1.
- Angevine, W. M., et al. (2013), Pollutant transport among California regions, *J. Geophys. Res. Atmos.*, **118**, 6750–6763, doi:10.1002/jgrd.50490.
- Bahreini, R., et al. (2012), Gasoline emissions dominate over diesel in formation of secondary organic aerosol mass, *Geophys. Res. Lett.*, **39**, L06805, doi:10.1029/2011GL050718.
- Bates, T. S., et al. (2012), Measurements of ocean derived aerosol off the coast of California, *J. Geophys. Res.*, **117**, D00V15, doi:10.1029/2012JD017588.
- Bauer, S. E., S. Menon, D. Koch, T. C. Bond, and K. Tsigaridis (2010), A global modeling study on carbonaceous aerosol microphysical characteristics and radiative effects, *Atmos. Chem. Phys.*, **10**, 7439–7456, doi:10.5194/acp-10-7439-2010.
- Baumgardner, D., G. L. Kok, and G. Raga (2004), Warming of the Arctic lower stratosphere by light absorbing particles, *Geophys. Res. Lett.*, **31**, L06117, doi:10.1029/2003GL018883.
- Bond, T. C. (2007), Can warming particles enter global climate discussions?, *Environ. Res. Lett.*, **2**(4), 045030, doi:10.1088/1748-9326/2/4/045030.
- Bond, T. C., G. Habib, and R. W. Bergstrom (2006), Limitations in the enhancement of visible light absorption due to mixing state, *J. Geophys. Res.*, **111**, D20211, doi:10.1029/2006JD007315.
- Bond, T. C., et al. (2013), Bounding the role of black carbon in the climate system: A scientific assessment, *J. Geophys. Res. Atmos.*, **118**, 5380–5552, doi:10.1002/jgrd.50171.
- Buffaloe, G. M., et al. (2014), Black carbon emissions from in-use ships: A California regional assessment, *Atmos. Chem. Phys.*, **14**, 1881–1896, doi:10.5194/acp-14-1881-2014.
- Canagaratna, M. R., et al. (2007), Chemical and microphysical characterization of ambient aerosols with the Aerodyne aerosol mass spectrometer, *Mass Spectrom. Rev.*, **26**, 185–222.
- Canagaratna, M. R., et al. (2015a), Elemental ratio measurements of organic compounds using aerosol mass spectrometry: Characterization, improved calibration, and implications, *Atmos. Chem. Phys.*, **15**, 253–272, doi:10.5194/acp-15-253-2015.
- Canagaratna, M. R., et al. (2015b), Chemical compositions of black carbon particle cores and coatings via soot particle aerosol mass spectrometry with photoionization and electron ionization, *J. Phys. Chem. A*, doi:10.1021/jp510711u.
- Cappa, C. D., et al. (2012), Radiative absorption enhancements due to the mixing state of atmospheric black carbon, *Science*, **337**, 1078, doi:10.1126/science.1223447.
- Cappa, C. D., et al. (2013), Response to comment on “Radiative absorption enhancements due to the mixing state of atmospheric black carbon”, *Science*, **339**, 393, doi:10.1126/science.1230260.
- Cappa, C. D., et al. (2014), A case study into the measurement of ship emissions from plume intercepts of the NOAA ship *Miller Freeman*, *Atmos. Chem. Phys.*, **14**, 1337–1352, doi:10.5194/acp-14-1337-2014.
- Corbin, J. C., B. Sierau, M. Gysel, M. Laborde, A. Keller, J. Kim, A. Petzold, T. B. Onasch, U. Lohmann, and A. A. Mensah (2014), Mass spectrometry of refractory black carbon particles from six sources: Carbon-cluster and oxygenated ions, *Atmos. Chem. Phys.*, **14**(5), 2591–2603, doi:10.5194/acp-14-2591-2014.

- DeCarlo, P. F., et al. (2006), Field-deployable, high-resolution, time-of-flight aerosol mass spectrometer, *Anal. Chem.*, *78*, 8281–8289.
- de Gouw, J., and C. Warneke (2007), Measurements of volatile organic compounds in the Earth's atmosphere using proton-transfer reaction mass spectrometry, *Mass Spectrom. Rev.*, *26*, 223–257.
- Docherty, K. S., et al. (2011), The 2005 Study of Organic Aerosols at Riverside (SOAR-1): Instrumental intercomparisons and fine particle composition, *Atmos. Chem. Phys.*, *11*, 12,387–12,420, doi:10.5194/acp-11-12387-2011.
- Farmer, D. K., A. Matsunaga, K. S. Docherty, J. D. Surratt, J. H. Seinfeld, P. J. Ziemann, and J. L. Jimenez (2010), Response of an aerosol mass spectrometer to organonitrates and organosulfates and implications for atmospheric chemistry, *Proc. Natl. Acad. Sci. U.S.A.*, *107*(15), 6670–6675, doi:10.1073/pnas.0912340107.
- Gao, R. S., et al. (2007), A novel method for estimating light-scattering properties of soot aerosols using a modified single-particle soot photometer, *Aerosol Sci. Technol.*, *41*, 125–135.
- Hayes, P. L., et al. (2013), Organic aerosol composition and sources in Pasadena, California during the 2010 CalNex campaign, *J. Geophys. Res. Atmos.*, *118*, 9233–9257, doi:10.1002/jgrd.50530.
- Huffman, J. A., P. J. Ziemann, J. T. Jayne, D. R. Worsnop, and J. L. Jimenez (2008), Development and characterization of a fast-stepping/scanning thermomuder for chemically-resolved aerosol volatility measurements, *Aerosol Sci. Technol.*, *42*, 395–407, doi:10.1080/02786820802104981.
- Huffman, J. A., et al. (2009), Chemically-resolved aerosol volatility measurements from two megacity field studies, *Atmos. Chem. Phys.*, *9*, 7161–7182, doi:10.5194/acp-9-7161-2009.
- Intergovernmental Panel on Climate Change (2013), *Climate Change 2013, The Physical Science Basis. Contribution of Working Group I to the Fifth Assessment Report of the Intergovernmental Panel on Climate Change*, edited by T. F. Stocker et al., 1535 pp., Cambridge Univ. Press, Cambridge, U. K., and New York.
- Jacobson, M. Z. (2001), Strong radiative heating due to the mixing state of black carbon in atmospheric aerosols, *Nature*, *409*, 695–697.
- Jacobson, M. Z. (2006), Effects of externally-through-internally-mixed soot inclusions within clouds and precipitation on global climate, *J. Phys. Chem. A*, *110*(21), 6860–6873, doi:10.1021/jp056391r.
- Jimenez, J. L., et al. (2009), Evolution of organic aerosols in the atmosphere, *Science*, *326*, 1525–1529, doi:10.1126/science.1180353.
- Lack, D. A., and C. D. Cappa (2010), Impact of brown and clear carbon on light absorption enhancement, single scatter albedo and absorption wavelength dependence of black carbon, *Atmos. Chem. Phys.*, *10*, 4207–4220, doi:10.5194/acp-10-4207-2010.
- Lack, D. A., M. S. Richardson, D. Law, J. M. Langridge, C. D. Cappa, R. J. McLaughlin, and D. M. Murphy (2012), Aircraft instrument for comprehensive characterization of aerosol optical properties, Part 2: Black and brown carbon absorption and absorption enhancement measured with photo acoustic spectroscopy, *Aerosol Sci. Technol.*, *46*(5), 555–568, doi:10.1080/02786826.2011.645955.
- Langridge, J. M., M. S. Richardson, D. Lack, D. Law, and D. M. Murphy (2011), Aircraft instrument for comprehensive characterization of aerosol optical properties, Part I: Wavelength-dependent optical extinction and its relative humidity dependence measured using cavity ringdown spectroscopy, *Aerosol Sci. Technol.*, *45*(11), 1305–1318, doi:10.1080/02786826.2011.592745.
- Lu, R., and R. P. Turco (1996), Ozone distributions over the Los Angeles Basin: Three dimensional simulations with the SMOG model, *Atmos. Environ.*, *30*, 4155–4176.
- Massoli, P., et al. (2012), Pollution gradients and chemical characterization of particulate matter from vehicular traffic near major roadways: Results from the 2009 Queens College Air Quality study in NYC, *Aerosol Sci. Technol.*, *46*, 1201–1218.
- Matthew, B. M., A. M. Middlebrook, and T. B. Onasch (2008), Collection efficiencies in an Aerodyne aerosol mass spectrometer as a function of particle phase for laboratory generated aerosols, *Aerosol Sci. Technol.*, *42*(11), 884–898, doi:10.1080/02786820802356797.
- McMeeking, G. R., et al. (2010), Black carbon measurements in the boundary layer over western and northern Europe, *Atmos. Chem. Phys.*, *10*, 9393–9414, doi:10.5194/acp-10-9393-2010.
- Metcalfe, A. R., J. S. Craven, J. J. Ensberg, J. Brioude, W. Angevine, A. Sorooshian, H. T. Duong, H. H. Jonsson, R. C. Flagan, and J. H. Seinfeld (2012), Black carbon aerosol over the Los Angeles Basin during CalNex, *J. Geophys. Res.*, *117*, D00V13, doi:10.1029/2011JD017255.
- Middlebrook, A. M., R. Bahreini, J. L. Jimenez, and M. R. Canagaratna (2012), Evaluation of composition-dependent collection efficiencies for the Aerodyne Aerosol Mass Spectrometer using field data, *Aerosol Sci. Technol.*, *46*(3), 258–271, doi:10.1080/02786826.2011.620041.
- Ng, N. L., et al. (2010), Organic aerosol components observed in Northern Hemispheric datasets from aerosol mass spectrometry, *Atmos. Chem. Phys.*, *10*, 4625–4641, doi:10.5194/acp-10-4625-2010.
- Onasch, T. B., A. Trimborn, E. C. Fortner, J. T. Jayne, G. L. Kok, L. R. Williams, D. R. Worsnop, and P. Davidovits (2012), Soot particle aerosol mass spectrometer: Development, application and initial validation, *Aerosol Sci. Technol.*, *46*, 804–817, doi:10.1080/02786826.2012.663948.
- Paatero, P., and U. Tapper (1994), Positive matrix factorization: A non-negative factor model with optimal utilization of error estimates of data values, *Environmetrics*, *5*, 111–126.
- Ramanathan, V., and G. Carmichael (2008), Global and regional climate changes due to black carbon, *Nat. Geosci.*, *1*(4), 221–227, doi:10.1038/ngeo156.
- Ramanathan, V., M. V. Ramana, G. Roberts, D. Kim, C. Corrigan, C. Chung, and D. Winker (2007), Warming trends in Asia amplified by brown cloud solar absorption, *Nature*, *448*(7153), 575–578, doi:10.1038/nature06019.
- Riemer, N., M. West, R. A. Zaveri, and R. C. Easter (2010), Estimating soot aging time scales with a particle-resolved aerosol model, *J. Aerosol Sci.*, *41*, 143–158, doi:10.1016/j.jaerosci.2009.08.009.
- Ryerson, T. B., et al. (2013), The 2010 California Research at the Nexus of Air Quality and Climate Change (CalNex) field study, *J. Geophys. Res. Atmos.*, *118*, 5830–5866, doi:10.1002/jgrd.50331.
- Schnaiter, M., C. Linke, O. Möhler, K. Naumann, H. Saathoff, R. Wagner, U. Schurath, and B. Wehner (2005), Absorption amplification of black carbon internally mixed with secondary organic aerosol, *J. Geophys. Res.*, *110*, D19204, doi:10.1029/2005JD006046.
- Schwarz, J. P., et al. (2006), Single-particle measurements of midlatitude black carbon and light-scattering aerosols from the boundary layer to the lower stratosphere, *J. Geophys. Res.*, *111*, D16207, doi:10.1029/2006JD007076.
- Schwarz, J. P., et al. (2008a), Measurement of the mixing state, mass, and optical size of individual black carbon particles in urban and biomass burning emissions, *Geophys. Res. Lett.*, *35*, L13810, doi:10.1029/2008GL033968.
- Schwarz, J. P., et al. (2008b), Coatings and their enhancement of black carbon light absorption in the tropical atmosphere, *J. Geophys. Res.*, *113*, D03203, doi:10.1029/2007JD009042.
- Sedlacek, A. J., III, E. R. Lewis, L. Kleinman, J. Xu, and Q. Zhang (2012), Determination of and evidence for non-core shell structure of particles containing black carbon using the Single-Particle Soot Photometer (SP2), *Geophys. Res. Lett.*, *39*, L06802, doi:10.1029/2012GL050905.
- Shindell, D., et al. (2012), Simultaneously mitigating near-term climate change and improving human health and food security, *Science*, *335*, 183–189, doi:10.1126/science.1210026.
- Stephens, M., N. Turner, and J. Sandberg (2003), Particle identification by laser-induced incandescence in a solid-state laser cavity, *Appl. Opt.*, *42*(19), 3726–3736, doi:10.1364/AO.42.003726.

- Stier, P., J. H. Seinfeld, S. Kinne, and O. Boucher (2007), Aerosol absorption and radiative forcing, *Atmos. Chem. Phys.*, *7*, 5237–5261, doi:10.5194/acp-7-5237-2007.
- Subramanian, R., et al. (2010), Black carbon over Mexico: The effect of atmospheric transport on mixing state, mass absorption cross-section, and BC/CO ratios, *Atmos. Chem. Phys.*, *10*, 219–237, doi:10.5194/acp-10-219-2010.
- Sueper, D. (2010), ToF-AMS analysis software. [Available at <http://cires.colorado.edu/jimenez-group/ToFAMSResources/ToFSoftware/index.html>.]
- Ulbrich, I. M., M. R. Canagaratna, Q. Zhang, D. R. Worsnop, and J. L. Jimenez (2009), Interpretation of organic components from positive matrix factorization of aerosol mass spectrometric data, *Atmos. Chem. Phys.*, *9*, 2891–2918.
- Villani, P., D. Picard, V. Michaud, P. Laj, and A. Wiedensohler (2008), Design and validation of a volatility hygroscopic tandem differential mobility analyzer (VH-TDMA) to characterize the relationships between the thermal and hygroscopic properties of atmospheric aerosol particles, *Aerosol Sci. Technol.*, *42*, 729–741.
- Wagner, N. L., et al. (2012), The sea breeze/land breeze circulation in Los Angeles and its influence on nitryl chloride production in this region, *J. Geophys. Res.*, *117*, D00V24, doi:10.1029/2012JD017810.
- Willis, M. D., A. K. Y. Lee, T. B. Onasch, E. C. Fortner, L. R. Williams, A. T. Lambe, D. R. Worsnop, and J. P. D. Abbatt (2014), Collection efficiency of the Soot-Particle Aerosol Mass Spectrometer (SP-AMS) for internally mixed particulate black carbon, *Atmos. Meas. Tech.*, *7*, 4507–4516, doi:10.5194/amt-7-4507-2014.
- Zhang, Q., M. R. Alfarra, D. R. Worsnop, J. D. Allan, H. Coe, M. R. Canagaratna, and J. L. Jimenez (2005a), Deconvolution and quantification of hydrocarbon-like and oxygenated organic aerosols based on aerosol mass spectrometry, *Environ. Sci. Technol.*, *39*, 4938–4952, doi:10.1021/es048568l.
- Zhang, Q., M. R. Canagaratna, J. T. Jayne, D. R. Worsnop, and J. L. Jimenez (2005b), Time and size-resolved chemical composition of submicron particles in Pittsburgh—Implications for aerosol sources and processes, *J. Geophys. Res.*, *110*, D07S09, doi:10.1029/2004JD004649.
- Zhang, Q., D. R. Worsnop, M. R. Canagaratna, and J. L. Jimenez (2005c), Hydrocarbon-like and oxygenated organic aerosols in Pittsburgh: Insights into sources and processes of organic aerosols, *Atmos. Chem. Phys.*, *5*, 3289–3311.
- Zhang, Q., J. L. Jimenez, M. R. Canagaratna, I. M. Ulbrich, N. L. Ng, D. R. Worsnop, and Y. Sun (2011), Understanding atmospheric organic aerosols via factor analysis of aerosol mass spectrometry: A review, *Anal. Bioanal. Chem.*, *401*, 3045–3067, doi:10.1007/s00216-011-5355-y.